JOURNAL OF GEOPHYSICAL RESEARCH, VOL. 87, NO. B2, PAGES 1001–1014, FEBRUARY 10, 1982

Thermal Isostasy: Response of a Moving Lithosphere to a Distributed Heat Source

DAVID T. SANDWELL

Department of Earth and Space Sciences, University of California at Los Angeles
Los Angeles, California 90024

Spreading ridges and hot spot swells are identified by their high surface heat flow, shallow seafloor, and high geopotential. To understand these and other thermotectonic features, the oceanic lithosphere is modeled as a thermomechanical boundary layer moving through a three-dimensional, time-independent heat source. The heat source mimics the heat advection associated with a spreading ridge or hot spot without introducing the nonlinearities of these flow processes. The Fourier transforms of three Green's functions (response functions), which relate the three observable fields to their common heat source, are determined analytically. Each of these reponse functions is highly anisotropic because the lithosphere is moving with respect to the source. However, the ratio of the gravity response function to the topography response function (i.e., gravity/topography transfer function) is nearly isotropic and has a maximum lying between the flexural wavelength and 2π times the thickness of the thermal boundary layer. The response functions are most useful for determining the surface heat flow, seafloor topography, and geopotential for complex lithospheric thermal structures. In practice, these three observables are calculated by multiplying the Fourier transform of the heat source by the appropriate response function and inverse transforming the products. Almost any time-independent thermotectonic feature can be modeled using this technique. Included in this report are examples of spreading ridges and thermal swells, although more complex geometries such as ridges offset by transform faults and RRR-type triple junctions can also be modeled. Because forward modeling is both linear and computationally simple, the inverse of this technique could be used to infer some basic characteristics of the heat source directly from the observed fields.

1. INTRODUCTION

The thermal and mechanical properties of the oceanic lithosphere have been largely determined by modeling seafloor depth, surface heat flow, and geopotential. Intrinsic thermal properties such as coefficient of thermal expansion, thermal diffusivity, and mantle temperature are inferred by modeling the observed age dependence of depth, heat flow, and geoid height [*Sclater and Francheteau,* 1970; *Sclater et al.,* 1975; *Parsons and Sclater,* 1977; *Sandwell and Schubert,* 1980]. According to the lithospheric cooling models [*Turcotte and Oxburgh,* 1967; *McKenzie,* 1967; *Parker and Oldenburg,* 1973; *Haxby and Turcotte,* 1978] significant variations in these observable fields occur over distances greater than the thickness of the thermal boundary layer. This indicates that lithospheric thermal properties are most sensitive to the longer wavelength variations in the observable fields. On the other hand, the rheology of the lithosphere is most strongly reflected in topography and free-air gravity anomaly at wavelengths near the flexural wavelength [*Walcott,* 1970; *McKenzie and Bowin,* 1976; *Watts,* 1978; *Caldwell and Turcotte,* 1979; *Chapple and Forsyth,* 1979; *McNutt,* 1979]. The combination of these studies, at long and short wavelengths, demonstrates that the oceanic lithosphere is a thermomechanical boundary layer. The thermal boundar layer (TBL) develops and increases in thickness as a consequence of conductive heat loss. A mechanical boundary layer develops concurrently with the TBL because creep processes are highly dependent upon temeprature [*Kirby,* 1980]. To a first approximation, the uppermost portion of the lithosphere, between depths of 10 and 40 km, has a viscous relaxation time that is greater than the age of the lithosphere and can maintain the large bending stresses (~50 MPa) associated with lithospheric flexure. Between the base of this elastic layer and the lithosphere-asthenosphere boundary, lies material with a plastic rheology that flows when it is subjected to the larger flexural stresses but is rigid enough to maintain the smaller, thermally induced stresses that support the difference in elevation between ridge crests and ocean basins [*Turcotte and Oxburgh,* 1976; *Kirby,* 1980; *Lambeck and Nakiboglu,* 1980]. The asthenosphere, which readily flows over geologic time, lies beneath this plastic layer.

In this study we develop a combined thermomechanical model for the oceanic lithosphere that is based upon the successful aspects of the longer-wavelength lithospheric cooling models and the shorter-wavelength flexure models. Our major purpose is to calculate the observables (surface heat flow, seafloor topography, and geopotential) for three-dimensional thermotectonic features without resorting to numerical methods (i.e., finite difference or finite element techniques).

The addition of a third dimension makes it possible to model features such as hot spot swells, offset spreading ridges, and RRR (ridge-ridge-ridge) type triple junctions. However, to maintain mathematical simplicity and linearity in the model, a number of physical processes are neglected or approximated. First, we assume that the flexural rigidity is not temperature dependent. This assumption is valid as long as the temperatures of the upper third of the lithosphere do not change significantly across the region being modeled. Second, we assume that perturbations to the observable fields result from thermal anomalies within the lithosphere. This assumption cannot be justified, since small-scale convection beneath a mature lithosphere has an effect upon both the seafloor topography and the geopotential [*McKenzie,* 1977; *Kaula,* 1980]. However, it is difficult to estimate these effects since the thermal and mechanical properties of the mantle are not well constrained [*Hager and O'Connell,* 1981]. In this model we consider only the lithospheric

Paper number 1B1614.
0148-0227/82/001B-1614$01.00

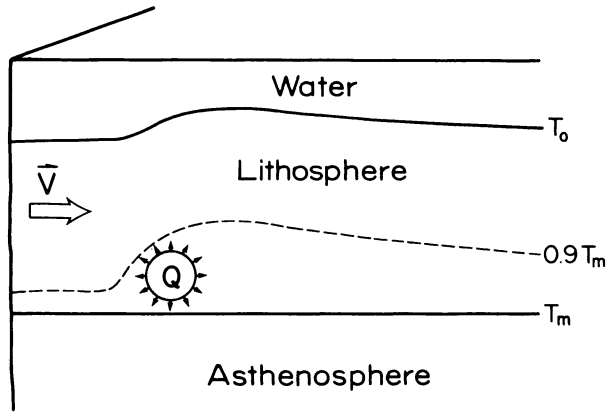

Fig. 1. As the lithosphere passes through a distributed heat source, at a velocity v it is heated, causing thermal expansion. The increase in surface heat flow far downstream from the source lowers the temperature perturbation, and the swell begins to subside. The base of the lithosphere, defined by the T_m isotherm, remains at a depth l.

contribution to the observable fields and assume that any portions of the observed fields that are incompatible with this model are, indeed, associated with mantle flow.

Heat advection from the upper mantle to the lithosphere is simulated by embedding a stationary time-independent heat source within the moving lithosphere. Clearly, this situation is physically unreasonable since the heat source will be swept downstream by the moving lithosphere. As an alternative, the source could be distributed along the base of the lithosphere. However, for velocities greater than a few millimeters per year, a basal heat source does not significantly alter the lithospheric thermal structure because downstream heat advection dominates vertical heat diffusion [*Birch,* 1975; *Gass et al.,* 1978; *Pollack et al.,* 1981]. To produce the rapid uplift rate at the southeast end of the Hawaiian swell, heat must be advected into the lower two thirds of the lithosphere [*Detrick and Crough,* 1978]. Instead of modeling this flow process, we have bypassed the problem by introducing a heat source within the moving lithosphere. This heat source representation not only retains linearity in the thermomechanical model but also allows creation of lithospheric thermal structures that are identical to the more reasonable flow models. In fact, any imaginable time-independent thermal structure can be created by a suitable heat source.

Perhaps that most severe restriction of the model is the assumption of a time-independent heat source, since it is evident that major plates have changed velocity, both amplitude and direction [*Menard and Atwater,* 1968]. The Hawaiian-Emperor seamount chain reflects the direction change of the Pacific plate with respect to the Hawaiian hot spot. For the past 40 m.y., however, this relative velocity has remained constant; to a first approximation, our proposed model may be applied. The heat source response is linear, so the effects of time variations in velocity, which are equivalent to space-time variations in heat source strength, could be approximated by superposition of a number of time-independent models. Alternatively, the problem could be reformulated with a time-dependent source. We have not added this fourth dimension, however, since time-dependent effects are not well constrained by the observations.

In section 2 we present a linear thermomechanical model for the oceanic lithosphere and develop analytic expressions for the Fourier transforms of three Green's functions (i.e., response functions) that relate the three observable fields to a lithosphere moving through a distributed heat source. Each of the observable fields is a three-dimensional convolution of the heat source with the appropriate Green's function. In the Fourier transform domain the convolution is just a multiplication, and the problem is naturally divided into a source function and a response function. The forms of these solutions lend themselves to three commonly used modeling techniques: transfer function modeling, forward modeling, and inverse modeling. Examples of each of these techniques are presented in sections 3, 4, and 5, respectively, to demonstrate the capabilities and limitations of the model. In section 3 we compare the gravity/topography transfer function for this thermal compensation model to the transfer functions for Airy and regional compensation models. Forward models of symmetrically spreading ridges and hot spot swells are presented in section 4. Finally, in section 5 we discuss the application of the response functions to the inverse problem, which is to infer basic characteristics of the heat source directly from the observables.

2. Response of a Moving Plate to a Distributed Heat Source

The thermomechanical model consists of a plate of thickness l moving at a constant velocity v through a three-dimensional, time-independent heat source, as shown in Figure 1. Far upstream from the source (i.e., v direction) the surface heat flow, seafloor topography, and gravitational potential are all zero. As the lithosphere passes through the source, its temperature increases. This produces a local increase in the observable fields. The amplitude and geometry of the field perturbations depend not only upon the shape and extent of the heat source but also upon the rheology and thermal properties of the lithosphere.

These properties and the boundary conditions are shown in Figure 2. The top of the lithosphere is maintained at a temperature of T_0, while the base of the lithosphere, at a depth l, has a temperature T_m. The intrinsic thermal properties α, κ, and C_p (see Table 1 for definitions and values of these parameters) are assumed to remain constant throughout the lithosphere. Figure 2*b* shows the rheology of our model lithosphere. The uppermost layer behaves like a thin

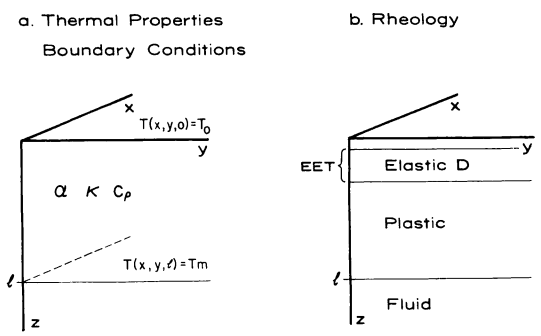

Fig. 2. (*a*) Intrinsic thermal properties and thermal boundary conditions. The temperature at the seafloor is T_0 and at the base of the lithosphere is T_m. The thermal properties α, κ, and C_p are constant throughout the lithosphere. (*b*) The lithosphere has an elastic layer with a flexural ridigity of D and a plastic layer that extends to the base of the TBL.

elastic plate with a flexural rigidity of D. Beneath it lies a plastic layer that can support stresses arising from thermal buoyancy but cannot support the larger deviatoric stresses associated with lithospheric flexure. The asthenosphere lies at depths greater than l and behaves as an incompressible, inviscid fluid. The mechanical boundary conditions are the vertical seafloor displacement $w(\mathbf{x})$ and its derivatives must vanish as $|\mathbf{x}| \rightarrow \infty$. In the absence of a heat source, the temperature increases linearly with increasing depth from a value of T_0 at $z = 0$ to T_m at $z = l$. As the lithosphere passes through the source, it heats up; maximum temperatures are attained on the downstream edge of the source. Away from the upper and lower boundaries the temperatures are constrained only by the heat source and could rise above T_m or fall below T_0 if the source is not designed properly.

Expressions relating the surface observables and the temperature perturbation to an arbitrary heat source are derived in Appendix A. The solution proceeds in a straightforward manner. The temperature perturbation is found by solving the inhomogeneous heat conduction equation for a plate moving through a heat source. The surface heat flow is the thermal conductivity multiplied by the surface temperature gradient. Downstream from the source lies a low-density, buoyant region that exerts an upward force upon the base of the elastic layer. The vertical seafloor deflection is determined by solving the biharmonic equation for a thin elastic plate overlying a fluid half space where the inhomogeneous pressure term is the integral over depth of the thermal buoyancy force. The combination of the mass excess contained in the seafloor swell and the mass deficit supporting the swell perturbs the gravitational potential. Well-known Greens' functions exist for each of the differential equations (i.e., the diffusion equation, the biharmonic equation, and Poisson's equation). Thus, the observable fields could be calculated by multiple, three-dimensional convolutions over these Green's functions. However, many of the integrals can only be performed numerically. To avoid this time-consuming procedure, each of the Green's functions is Fourier-transformed in the $\hat{x}$ and $\hat{y}$ directions. This reduces the multiple x and y convolutions to multiplications. The remaining vertical convolution integrals are all simple enough to be evaluated analytically.

A flat earth approximation is used throughout the derivation. The error introduced in the gravitational potential by this approximation can be estimated from the ratio of the spherical upward continuation kernel to the flat earth upward continuation kernel for isostatically compensated topography [see *Jeffreys*, 1976, p. 237]:

$$\left(\frac{2n}{(2n+1)}\right)\left(\frac{1-(1-h/a)^n}{1-\exp(-nh/a)}\right) \tag{1}$$

where n is the spherical harmonic degree, a is the radius of the earth, and h is the depth of compensation. This ratio is shown in Figure 3 (solid circles) for $h = 100$ km. Most of the difference between the two upward continuation kernels comes from the factor $2n/(2n + 1)$ [*Dorman and Lewis*, 1970]. The crosses on Figure 3 show this ratio with the factor omitted. This 'isostatic earth-flattening factor' was included in the derivation of the gravitational potential and substantially reduces the error associated with the flat earth approximation.

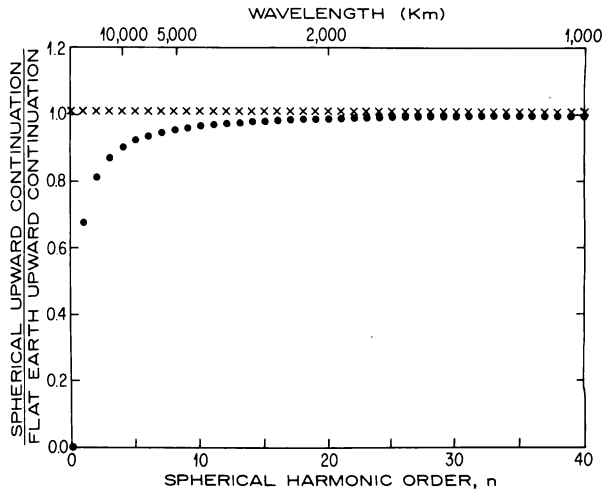

Fig. 3. The ratio of the spherical upward continuation kernel to the flat earth upward continuation kernel for topography that is isostatically compensated at a depth of 100 km is plotted (solid circles) against spherical harmonic order n. The same ratio with the factor $2n/(2n + 1)$ removed is shown as crosses.

The two-dimensional Fourier transforms of the temperature perturbation $T(\mathbf{k}, z)$, the surface heat flow $Q(\mathbf{k})$, the seafloor topography $W(\mathbf{k})$, and the gravitational potential $U(\mathbf{k})$ are equal to the vertical convolution of the heat source $q(\mathbf{k}, z)$ with their respective response functions. These convolution integrals are given in equations (A11), (A14), (A19), and (A29) of Appendix A. Calculating the temperature perturbation and the observables from these equations requires a considerable amount of computation. For an arbitrary source, one must first take its Fourier transform at each depth, perform the vertical convolution, and take the inverse Fourier transform of the result. Computation time is vastly decreased if the heat source can be separated into horizontal and vertical components as follows:

$$q(\mathbf{x}, z) = q(\mathbf{x})\, f(z) \tag{2}$$

and if the vertical convolution of $f(z)$ with each of the response functions can be performed analytically.

The most useful source function decreases linearly with depth between either the seafloor and the base of the lithosphere or a depth z_1 and the base of the lithosphere:

$$\begin{aligned} f(z) &= 0 \qquad z < z_1 \\ f(z) &= 1 - z \qquad z_1 < z < l \end{aligned} \tag{3}$$

TABLE 1. Definitions and Values of Parameters

Parameter	Definition	Value/Units
a	mean earth radius	6371 km
α	thermal expansion coefficient	3.1×10^{-5} °C^{-1}
D	flexural rigidity	7×10^{22} N m
C_p	heat capacity	1172 J kg^{-1} °C^{-1}
g	acceleration of gravity	9.82 m s^{-2}
G	gravitational constant	6.67×10^{-11} N m^2 kg^{-2}
κ	thermal diffusivity	8×10^{-7} m^2 s^{-1}
l	lithospheric thickness	128 km
ρ_m	mantle density	3330 kg m^{-3}
ρ_w	water density	1025 kg m^{-3}
s	mean seafloor depth	5 km
T_m	mantle temperature	1365 °C
T_0	seafloor temperature	0°C

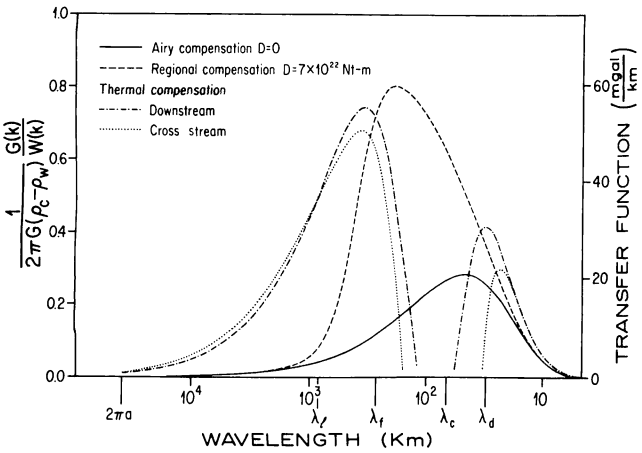

Fig. 4. Gravity/topography transfer functions for Airy compensation (solid line), regional compensation (dashed line), and thermal compensation (dashed-dotted line for downstream, dotted line for cross-stream). The five important length scales are λ_d = 31 km (2π × ocean depth), λ_c = 69 km (2π × depth to Moho), λ_f = 263 km (flexural wavelength), λ_l = 804 km (2π × depth to the asthenosphere), and $2\pi a$, where a is the radius of the earth.

As shown in the following sections, this particular depth variation can be used to construct a spreading ridge model or a lithospheric thinning model. Consider a thinning model. Far upstream from the source, the temperature increases linearly with depth. The lower portion of the lithosphere, between depths of z_1 and l, can be thinned (raised to a temperature approaching T_m) by a source that decreases linearly with depth according to (3). Equation (3) is also simple enough to be analytically convolved with each of the response functions. These convolutions are carried out in Appendix B. The results are given in equations (B2), (B3), (B4), and (B5), where the temperature and the observables $O_i(\mathbf{k})$ are related to the source $q(\mathbf{k})$ by multiplication with the appropriate response function $K_i'(\mathbf{k})$:

$$O_i(\mathbf{k}) = q(\mathbf{k})\, K_i'(\mathbf{k}) \tag{4}$$

The index i is equal to 0 for temperature, 1 for heat flow, 2 for topography, and 3 for potential. By performing these convolutions analytically the modeling procedure is reduced to two, two-dimensional Fourier transforms that can be calculated rapidly using the FFT algorithm (fast Fourier transform). For example, the geoid height over a lithosphere moving at velocity v through a source that varies with depth like (3) is calculated by taking the two-dimensional FFT of the source, multiplying by $K_3'(\mathbf{k})$, and inverse transforming the result.

In theory, this procedure is relatively simple. However, in practice, problems arise because the heat source must be represented on a grid with a finite number of points. To avoid aliasing the digital Fourier transform of the source, the spacing between grid points must be less than one half the shortest wavelength contained in the source. The width of the grid in the cross-stream direction must be at least twice the source width or the flexural wavelength, whichever is larger. In the downstream direction, the grid length must be $\gg l^2 v/\kappa$ so that the inverse FFT is not aliased by incomplete sampling in wave number space; we have used a grid length of 4×10^4 km in our models. This great length is required because it takes about one billion years for a heat pulse, within a 128-km-thick lithosphere, to decay to less than 1% of its initial value. Indeed, it is numerically impossible to calculate models when the plate thickness approaches infinity, since the grid must contain an infinite number of points in the downstream direction (L. M. Dorman, personal communication, 1980). However, if the shortest wavelength contained in the heat source is >1 km and the lithospheric thickness is <1000 km, then the modeling procedure is extremely fast.

Before presenting forward model calculations, it is useful to look at the ratio of the gravity response function (B6) to the topography response function (B5) in the wave number domain, since this ratio is independent of the horizontal heat source variations.

3. Gravity/Topography and Geoid/Topography Transfer Functions

Transfer functions or admittance functions have been used to determine the strength of the lithosphere. Since gravitational potential is nearly linearly related to topography in wave number space [*Lewis and Dorman,* 1970; *McNutt,* 1979], the ratio of the Fourier transform of the potential to the Fourier tranform of the topography contains information about the topographic compensation mechanism (e.g., local, regional, or thermal). The flexural rigidity of the elastic portion of the lithosphere has been estimated by fitting the observed transfer function to the transfer function predicted by the elastic plate model. The implicit assumption in transfer function modeling is that the perturbation to the gravitational potential is caused by a topographic load on the earth's surface [*Dorman and Lewis,* 1970]. In this case the source is the topographic load, the transmitter is the elastic plate model, and the receiver is the gravitational potential. However, for thermotectonic features such as spreading ridges and broad swells in the seafloor, the ultimate source of the gravitational potential is not the topographic load but is instead the thermal anomaly within the lithosphere. Therefore, it is not strictly legitimate to calculate the potential/topography transfer function for this model, and the quotient $U(\mathbf{k})/W(\mathbf{k})$ will not always be well behaved. Despite this difficulty, it is useful to compare this thermomechanical transfer function $R_T(\mathbf{k})$ with transfer functions for other types of compensation and also with observed transfer functions. Horizontal variations in the heat source are eliminated by taking the ratio of $U(\mathbf{k})$ to $W(\mathbf{k})$. This yields

$$R_T(\mathbf{k}) = K_3'(\mathbf{k})/K_2'(\mathbf{k}) \tag{5}$$

where K_2' and K_3' are given in (B5) and (B6), respectively.

A comparison of this thermal transfer function with the elastic plate transfer function demonstrates that the two compensation mechanisms are partially separated in wave number space. Figure 4 shows normalized gravity/topography transfer functions for the elastic plate model with flexural rigidities of zero, which corresponds to Airy-Heiskanen compensation (solid line), and 7×10^{22} N m, a typical value for oceanic lithosphere (*Watts* [1978]; dashed line). The important length scales for the elastic late model are reflected in the transfer function. For wavelengths less than λ_d (2π × ocean depth) the portion of the gravity field caused by undulations in the seafloor-water interface is attenuated by upward continuation. Similarly, λ_c (2π × depth to the crust-mantle interface) marks the shortest wavelength where the gravity field from Moho undulations can still be ob-

served. Accordingly, Airy-compensated topography has a transfer function peak lying between λ_d and λ_c. A larger value of flexural rigidity introduces another length scale, the flexural wavelength λ_f, which is related to the flexural rigidity by

$$\lambda_f = 2\pi\left[\frac{D}{g(\rho_m - \rho_w)}\right]^{1/4} \quad (6)$$

For wavelengths much less than λ_f the topography is strongly reflected in the gravity field, and therefore it appears 'uncompensated' (regionally compensated is a better term). The real part of the thermal transfer function for the downstream (dashed-dotted line) and cross-stream (dotted line) directions are also shown on Figure 4. The imaginary part of the downstream transfer function is only about 1% of the real part, while the cross-stream transfer function is purely real. This transfer function corresponds to a lithosphere that has been thinned from an initial depth of 128 km to a final depth of 40 km, using (3) for the vertical heat source variation. The main peak in the thermal transfer function occurs between λ_l ($2\pi \times$ depth to the asthenosphere) and λ_f (for this case $D = 7 \times 10^{22}$ N m). Looking from λ_f toward shorter wavelengths, the transfer function first becomes negative, then positive, and finally approaches zero. This rapid decline in the transfer function at the flexural wavelength occurs because the strength of the elastic layer does not allow the seafloor to flex under the thermal buoyancy force, and therefore the positive gravity field caused by the attenuated seafloor swell is not as strong as the negative field from the low-density root. At wavelengths less than λ_f, the strange behavior of the transfer function should be ignored, since for any reasonable heat source (i.e., one that does not melt the lithosphere anywhere) both the gravity and topography are too small to be observed.

The geoid height/topography transfer functions for these same models are shown in Figure 5. These geoid/topography transfer functions are enhanced at the longer wavelengths with respect to the gravity/topography transfer functions. The 'isostatic earth flattening factor' $2n/(2n + 1)$ forces the transfer functions to approach two thirds its maximum value as the wavelength approaches $2\pi \times$ radius of the earth.

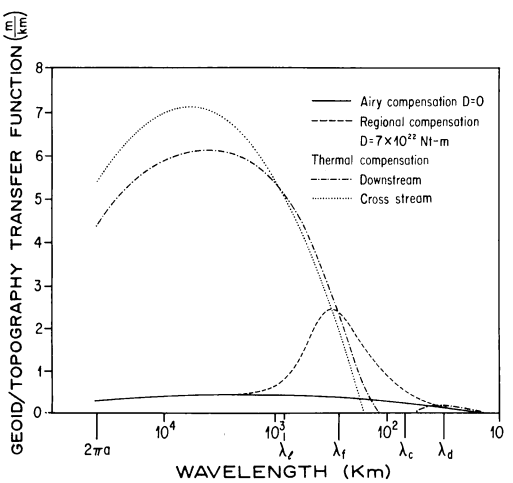

Fig. 5. Geoid/topography transfer functions for the same three models as shown in Figure 4. The thermal transfer function dominates the mechanical transfer function when $\lambda > \lambda_f$.

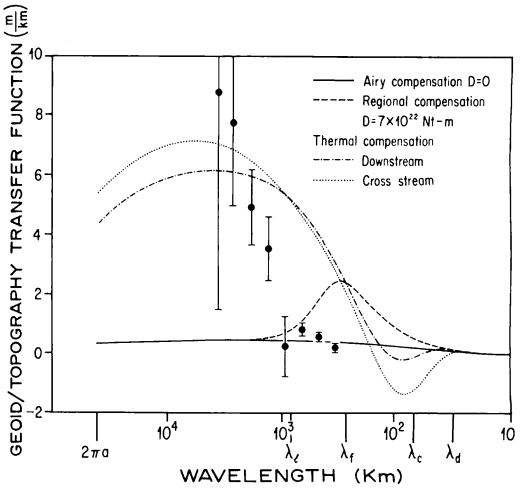

Fig. 6. Data points are estimates of the geoid/topography transfer function for a region in the central Pacific containing the Hawaiian swell. For wavelengths greater than 1100 km the data lie closest to the thermal transfer function, while at shorter wavelengths the topography appears to be Airy compensated.

Without this factor it would remain constant, as predicted by the Ockendon-Turcotte approximation [*Ockendon and Turcotte,* 1977].

A comparison of Figures 4 and 5 reveals the relative sensitivity of the free-air gravity data and geoid height data to various forms of compensation. For example, 1 km of thermally compensated topography with a wavelength of 3000 km will produce 10 mGal of gravity anomaly and 7 m of geoid height. At longer wavelengths, however, the gravity field diminishes, while the geoid amplitude remains relatively constant. At the other end of the spectrum, where $\lambda < \lambda_f$, the gravity anomaly is more sensitive to the mechanically compensated topography than the geoid height when measurement errors are considered [*Chapman and Talwani,* 1979]. Finally, near the flexural wavelength, the thermal transfer function $R_T(\mathbf{k})$ and the mechanical transfer function $R_M(\mathbf{k})$ must overlap. This region of overlap can lead to some difficulties when interpreting observed gravity/topography or geoid/topography transfer functions.

Sandwell and Poehls [1980] have calculated the geoid/topography transfer function for a region in the Central Pacific. The major topographic features included in this region are the Hawaiian swell, the Hawaiian Island chain, the Necker ridge, the northern end of the Line Islands, the Mid-Pacific mountains, and a number of fracture zones. Transfer function estimates and one standard deviation uncertainties are shown on Figure 6 along with the thermal and mechanical transfer functions from Figure 5. At wavelengths greater than 1100 km the data roughly follow the thermal compensation model, while at shorter wavelengths the data lie closer to the Airy compensation model. At intermediate wavelengths, however, the behavior of the observed transfer function can be understood by considering that some fraction of the topography is mechanically supported $W_M(\mathbf{k})$, while the remaining topography is thermally supported $W_T(\mathbf{k})$. The observed transfer function could be reproduced from a mixture of R_M and R_T:

$$R = R_M[W_M/(W_M + W_T)] + R_T[W_T/(W_M + W_T)] \quad (7)$$

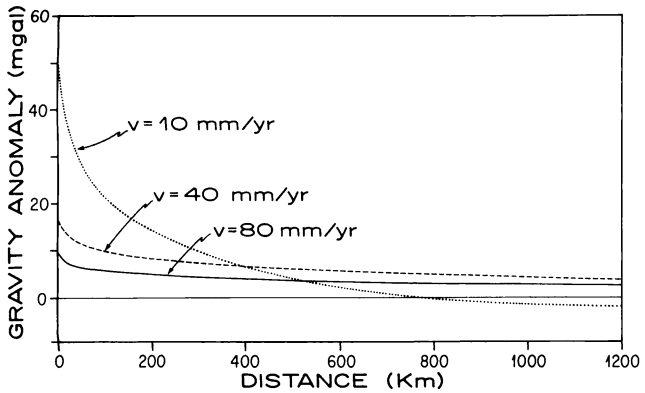

Fig. 7. Gravity anomaly versus distance from the ridge axis for half-spreading velocities of 10, 40, and 80 mm/yr.

There are an infinite number of ways to partition the topography amplitude spectrum between W_M and W_T. *Sandwel and Poehls* [1980] assumed that all of the topography with wavelengths greater than 1100 km was thermally compensated, while the remainder was Airy compensated. For this partitioning, the transfer function follows R_M for $\lambda <$ 1100 km and follows R_T for $\lambda >$ 1100 km. A more reasonable partitioning could be used to fit the data more precisely. Considering the uncertainty in the observed transfer function, a step function partitioning suffices.

The thermal compensation model provides a direct link between potential/topography transfer functions and a thermal perturbation within the lithosphere. However, to estimate the amplitudes of the observable quantities (i.e., heat flow, topography, free-air gravity, geoid height), it is best to look at the space domain response of the lithosphere to thermal perturbations of varying geometry. This is done in the next section, where we present forward model calculations for spreading ridge models and lithospheric thinning models.

4. Forward Models

Lithospheric Cooling Models

Lithospheric cooling models are presented here to demonstrate the utility of the heat source formulation and also to check our results against previously published results (i.e., depth and heat flow model, *McKenzie* [1967]; free-air gravity model, *Sclater and Francheteau* [1970], *Lambeck* [1972], and *Oldenburg* [1975]; geoid height model, *Sandwell and Schubert* [1980] and *Parsons and Richter* [1980]). To simulate the thermal structure of lithosphere leaving a spreading center at a velocity v_x, the initial linear temperature gradient is perturbed to a constant temperature with depth. This is accomplished by placing a heat source at the ridge crest that is infinite in the $\hat{y}$ direction, delta function like in the $\hat{x}$ direction (in practice, a narrow Gaussian function was used to avoid aliasing the FFT of the source) and decreases linearly with depth according to (3) with $z_1 = 0$. This heat source geometry produces only half of a spreading ridge. The other half is obtained by using only the real part of the complex response functions (i.e., forcing symmetry). The depth-age and heat flow–age relations are identical to those already published for the late spreading model (*Parsons and Sclater* [1977]; North Atlantic model) and therefore are not presented. The gravity anomaly versus distance from the ridge appears in Figure 7 for half-spreading rates of 10, 40, and 80 mm/yr. The amplitude of the gravity anomaly is nearly inversely proportional to the spreading velocity and correlates better with distance from the ridge axis than it does with seafloor age. On the other hand, the geoid height–age relation is nearly independent of spreading velocity, as shown in Figure 8. Thus, correlations of geoid height with age are useful in characterizing the actual thermal structure of a cooling lithosphere [*Haxby and Turcotte*, 1978; *Sandwell and Schubert*, 1980].

In our model, the heat source used to recreate the thermal structure of the plate spreading model has an infinite heat/volume supplied directly beneath the ridge axis. This delta function heat source (in $\hat{x}$ direction) produces a singularity in the surface heat flow and also causes the gravity anomaly to have a very sharp peak over the ridge. The response function technique allows a variable width heat source. A more reasonable width of 10 km [*Sleep and Rosendahl*, 1979] removes 10 mGal from the gravity peak for v_x = 10 mm/yr and at the same time lowers the ridge crest heat flow singularity to a finite value of 475 mW m^{-2}. Since the choice of the heat source geometry is totally arbitrary, more exotic spreading ridge models can be created.

As the lithosphere moves from the spreading ridge, it cools and thickens with age. If the growth of the TBL is uninterrupted by additional sources of heat, then the lithosphere and, consequently, the seafloor depth continue to increase as (age)$^{1/2}$, assuming that α and κ are constant throughout the lithosphere. However, in both the Atlantic and Pacific oceans the average depth-age relation begins to flatten from the prediction of the TBL model at about 70 m.y. [*Sclater et al.*, 1971; *Parsons and Sclater*, 1977]. In the next section we assume that this flattening is caused by heat transfer from the upper mantle to the base of the lithosphere. We then use our model to predict the shapes and amplitudes of the observable fields for various heat source geometries.

Lithospheric Reheating Models

The flattening of the depth-age relation can be explained by the plate cooling model [*McKenzie*, 1967] which as a constant temperature at the base of the lithosphere. According to this model, the lower temperature boundary condition is maintained by mantle-to-lithosphere heat transfer that

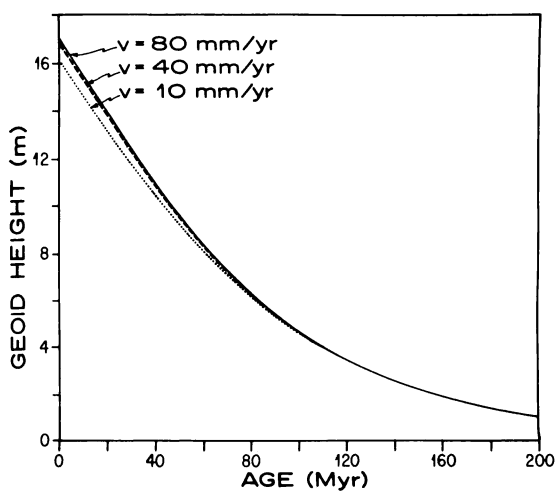

Fig. 8. Geoid height versus age for three spreading velocities. The geoid-age relation is nearly independent of spreading velocity for this cooling model.

increases monotonically with age. This age-dependent heat input has been modeled by a number of physical mechanisms including convective instability at the base of the lithosphere [*Parsons and McKenzie,* 1978] and an increase in shear heating with age as the lithosphere-asthenosphere boundary cools and becomes more viscous [*Schubert et al.,* 1976]. One must ask, however, is the heat input really age dependent? Surely, this cannot be determined from the depth-age relation, since by correlating depth with age, much of the information about spacial variations of depth is lost; this is especially true for the depth variations along isochrons. The space domain deviations of the depth, heat flow, and geoid from the predictions of the TBL model (i.e., residual depth, residual heat flow, and residual geoid anomalies) may, however, provide this information.

Residual depth maps have been computed for a large part of the world's oceans [*Menard,* 1973; *Sclater et al.,* 1975; *Cochran and Talwani,* 1977; *Menard and Dorman,* 1977; *Mammerickx,* 1981]. Thermal perturbations with characteristic wavelengths near 1000 km appear as topographic swells on residual depth maps (e.g., Bermuda swell, Hawaiian swell, Cape-Verde swell, Cook-Austral swell, etc.). These swells are also associated with an increase in geoid height [*Crough,* 1978] and an increase in heat flow [*Detrick et al.,* 1981]. Furthermore, hot spot swells are not preferentially located on older lithosphere. Indeed, if seafloor that has passed over a hot spot is excluded from the depth-age correlation, then depths increase as the $(\text{age})^{1/2}$ out to 90 m.y. [*Heestand and Crough,* 1981]. Hot spots provide an age-independent heat input and are partially responsible for the flattening of the depth-age relation.

In this section we simulate the effects of lithospheric reheating. Rather than focus on a particular reheating model such as small-scale convection, shear heating, or mantle plumes, we suggest dividing the off-ridge heat transfer according to its characteristic wavelength. The amplitudes of the observable fields are strongly dependent upon this wavelength. Forward modeling of various width heat sources provides a method for estimating the amplitudes of the surface observables and more importantly a means of determining which type of observable is best suited for studying thermal perturbations within a given wavelength band.

The responses of a moving lithosphere to thermal perturbations of three different characteristic wavelengths are shown in Figure 9. In these models, the lithosphere is thinned, using (3), to a depth of 40 km as it passes through a heat source at a velocity of 40 mm/yr. The source we have chosen varies as a Gaussian in both horizontal directions:

$$q(\mathbf{x}) = \left(\frac{\rho_m C_p v_x T_m f}{(2\pi)^{1/2}\sigma}\right) \exp\left(\frac{-(x^2 + y^2)}{2\sigma^2}\right) \qquad (8)$$

where 2σ is the source half width and f is a number <1 (temperatures may rise about T_m if $f > 1$). The source half widths for Figures 9*a*, 9*b*, and 9*c* are 2000, 200, and 60 km, respectively, and are outlined by circles. For comparison purposes, f was chosen so the maximum topographic swell produced by each of the three sources was 1.1 km when the lithospheric flexural rigidity was zero (local compensation). The maximum heat input per area for each of the sources is given in Table 2. To calculate the models shown in Figure 9, a typical value of flexural rigidity was used (7×10^{22} N m).

The top row in Figures 9*a*, 9*b*, and 9*c* shows the contours of temperature perturbation at a depth of 64 km. In each case the isotherms are swept downstream by the moving lithosphere. The maximum temperature is attained at a distance of 1σ to 2σ downstream from the heat source maximum. Contours of surface heat flow appear in the second row. The heat flow maxima are 19, 16, and 12 mW m and are displaced in time from the source peak by 32, 21, and 16 m.y. for Figures 9*a*, 9*b*, and 9*c*, respectively. The heat flow peak for the shortest-wavelength source has a relatively lower amplitude because a portion of the heat is conducted horizontally away from the source. The topography for the long- and intermediate-wavelength heat sources reaches a maximum of ~1 km at a distance of about 1σ *downstream* from the source peak. The smallest source, however, produces a maximum swell in the topography of less than 0.7 km and has a width that is much greater than the source half width. This relatively low amplitude accompanied by an increase in response wavelength occurs because the lithosphere does not bend readily at wavelengths shorter than its flexural wavelength.

The final two rows in Figures 9*a*, 9*b*, and 9*c* show contours of geoid height and free-air gravity anomaly. The peak response of the gravity field to the broadest heat source is only 8 mGal. Furthermore, the ratio of gravity to topography in the space domain is not constant but varies from 7 to 0 mGal/km. On the other hand, the geoid height closely resembles the topography and has a peak amplitude of 6.5 m. The intermediate-wavelength heat source produces a relatively large gravity anomaly (38 mGal) and 5.1 m of geoid height. The narrowest heat source (Figure 9*c*) produces a maximum gravity anomaly of 28 mGal, while the geoid height peak for this case is rather low (2.4 m). The effects of flexure are apparent in the intermediate- and short-wavelength gravity fields (the zero contour deviates from the others) but are absent in the geoid height contours.

The peak responses of the observables, heat flow, topography, gravity anomaly, and geoid height, are summarized in Table 2 for each of the three sources. A number of conclusions can be drawn about the observability of thermal perturbations in the lithosphere from these calculations.

1. A thermal perturbation with a characteristic wavelength much less than the flexural wavelength will be difficult to observe on maps of residual depth, residual geoid height, or residual gravity anomaly since the nonthermally compensated topography dominates at these wavelengths.

2. Thermal perturbations with characteristic wavelengths greater than λ_f (400 to 2000 km) have been observed in all of the data types and provide a basis for this lithospheric reheating model.

3. The longest-wavelength source (2σ = 2000 km) is reflected in the topography, heat flow, and geoid height but is absent in the gravity anomaly. Therefore, long-wavelength off-ridge lithospheric reheating will be observed on residual depth, residual heat flow, and possibly residual geoid height maps if reheating exists at this scale.

With the forward problem solved, the next step is to determine the class of acceptable heat sources that are compatible with the observed fields. As we have shown, the fields are linearly related to the source; thus, linear inverse theory can be used for this problem. These ideas are discussed in the next section.

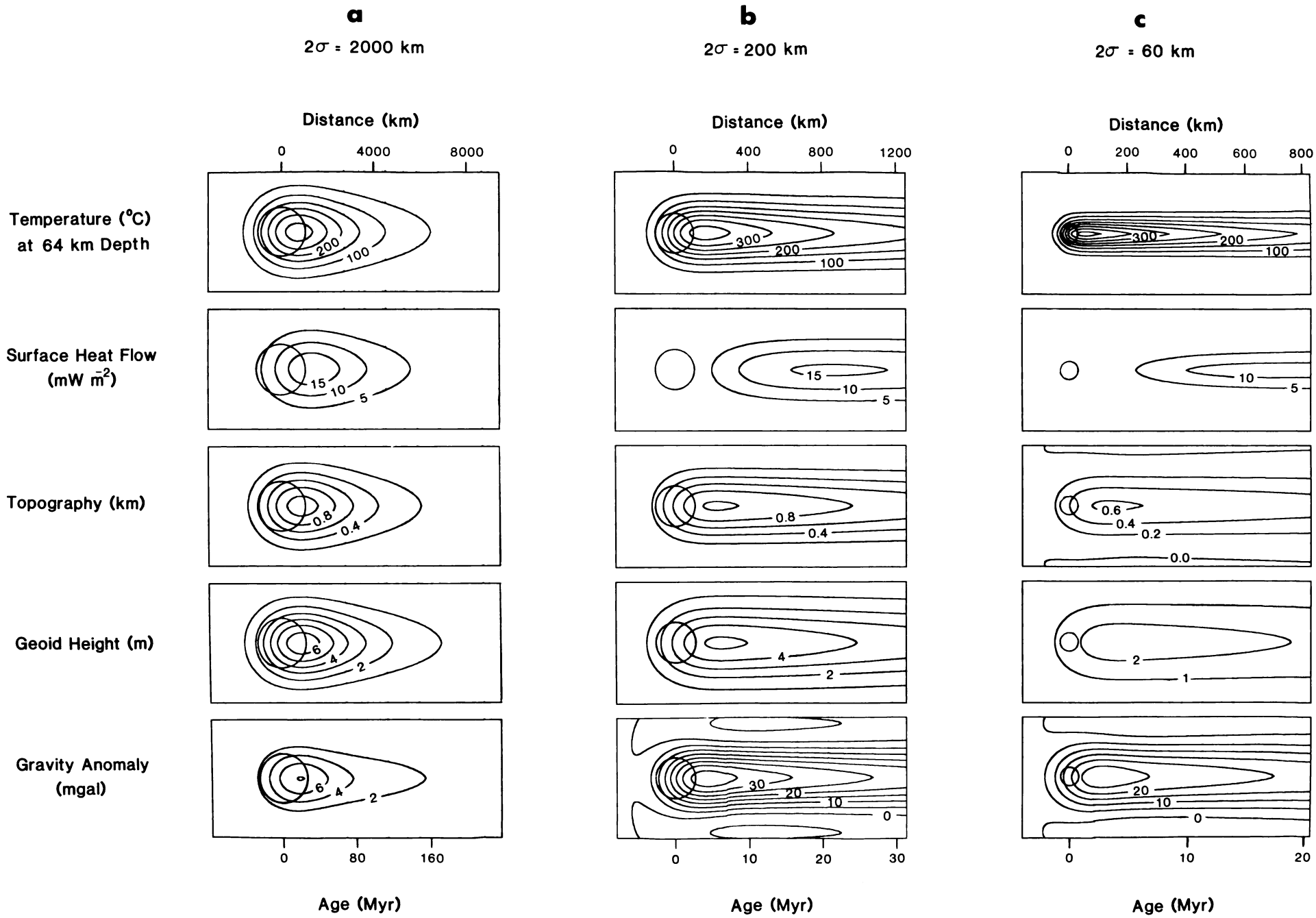
a
2σ = 2000 km
b
2σ = 200 km
c
2σ = 60 km
Distance (km)
0
4000
8000
400
800
1200
200
600
Temperature (°C) at 64 km Depth
Surface Heat Flow (mW m⁻²)
Topography (km)
Geoid Height (m)
Gravity Anomaly (mgal)
300
200
100
15
10
5
0.8
0.4
0.6
0.2
0.0
6
4
2
1
30
20
0
80
160
Age (Myr)

5. Inversion of Observables for Heat Sources

The proposed thermomechanical model for the oceanic lithosphere incorporates many assumptions and approximations. We have assumed that the intrinsic thermal and mechanical properties such as α, κ, C_p, and D are independent of temperature or pressure. Moreover, we assume that their values are accurately known from previous studies. The most severe model approximation is that the heat source is time independent. It is evident that plates change speed and direction on a time scale that is about equal to the time it takes a heat pulse to diffuse through the lithosphere. Indeed, this approximation limits the application of the model to the few regions where the thermal structure is steady state. Considering that little is known about lithospheric heating or reheating mechanisms, this approximate model may be useful.

For the moment, we assume that the model is a correct representation of the lithosphere. The solution to the forward problem shows that the vertical variation in the heat source $q(z_0)$ is related to the observables O_i by a linear transformation:

$$O_i(\mathbf{k}) = \int_0^1 q(\mathbf{k}, z_0)\, K_i(\mathbf{k}, z_0)\, dz_0 \qquad (9)$$

where $i = 1, 2, 3$. The $i = 1$ subscript corresponds to the heat flow, $i = 2$ corresponds to the topography, and $i = 3$ is the gravitational potential (see Appendix A, equations (A14), (A19), and (A29)). The inverse problem is to determine the three-dimensional variations in the heat source from the observations. Although the problem is linear, it is clearly nonunique for two reasons. First, (9) maps the function $q(z_0)$, which resides in an infinite dimensional space, into a three-dimensional data vector, and therefore the mapping is not one to one. Second, observations are made at only a finite number of points. Therefore, even if the data are errorless, the source cannot be uniquely defined. The problem is also unstable since the kernels of (9) are of the upward continuation type. It is impossible to determine the actual source function. However, the data may reveal its basic characteristics [*Parker*, 1977].

The first step in the problem is to minimize the class of acceptable solutions by applying a priori assumptions or constraints. For instance, the heat source should not oscillate from positive to negative in depth. Thus, a source that is responsible for a positive topographic swell should be positive and should not be composed of a large positive source overlying a smaller negative source. The class of acceptable models can be further restricted by requiring that the temperature of the lithosphere does not exceed the melting temperature. These constraints will greatly limit the class of acceptable heat source models.

Considering both the data inaccuracies and the inherent nonuniqueness of the inverse problem, it is probably best to either assume that the horizontal location of the source is known and invert for the depth dependence or assume that the depth dependence is known and solve for the horizontal variations. To solve either of these problems, the vertical and horizontal source variations must be decoupled:

$$q(\mathbf{k}, z_0) = q(\mathbf{k}) f(z_0) \qquad (10)$$

where $q(\mathbf{k})$ contains all of the horizontal variations and $f(z_0)$ is a function that depends on depth only. The second case, where $f(z_0)$ is known, could be used to locate off-ridge heat sources that are not associated with some obvious tectonic feature such as a linear island chain. With $f(z_0)$ known, the solution to (9) is just

$$q(\mathbf{k}) = O_i(\mathbf{k}) \left[\int_0^1 f(z_0)\, K_i(\mathbf{k}, z_0)\, dz_0 \right]^{-1} \qquad (11)$$

The three types of data can be used to estimate the uncertainties in $q(\mathbf{k})$; call them $\sigma_q(\mathbf{k})$. Both the horizontal variations in the source and its uncertainties can be mapped back into the space domain with the inverse Fourier transform. The spectral division in (11), however, is an unstable procedure since the denominator approaches zero at large wave numbers. Observational errors will appear as wild oscillations in the source function. To avoid these problems, spectral deconvolution techniques should be used [*Oldenburg*, 1981].

For a spreading ridge the horizontal location of the source is fairly well known since it coincides with the axial valley of the ridge crest. Equation (9) can be used to solve for the vertical dependence of the source. In this case, (9) becomes

$$O_i(\mathbf{k})/q(\mathbf{k}) = \int_0^1 f(z_0)\, K_i(\mathbf{k}, z_0)\, dz_0 \qquad (12)$$

where $q(\mathbf{k})$ is the Fourier transform of the ridge crest location. Each type of datum exists at only a finite number of wave numbers, say N. If i denotes the data type and j denotes a particular wave number $\mathbf{k}$, then (12) becomes

$$O_{ij}' = \int_0^1 f(z_0)\, K_{ij}(z_0)\, dz_0 \qquad (13)$$

where $O_{ij}' = O_{ij}/q_j$ and $K_{ij}(z_0)$ is the i kernel at the j wave number. The form of (13) is ideally suited for numerical inversion using the Backus-Gilbert [*Backus and Gilbert*, 1968] or spectral expansion [*Parker*, 1977] inversion techniques. Like other types of linear inverse problems there is a trade-off between model resolution and data misfit.

TABLE 2. Peak Responses of the Lithosphere to Gaussian Heat Sources

	Half Width of Source		
	2000 km	200 km	60 km
Maximum source strength, W m^{-2}	0.043	0.269	0.948
Temperature at 64-km depth, °C	320	375	423
Surface heat flow, mW m^{-2}	18.8	15.9	12.1
Seafloor topography, km	1.10	1.02	0.63
Geoid height, m	6.5	5.1	2.4
Gravity anomaly, mGal	8.0	37.8	28.3

Fig. 9. (opposite) The responses of the lithosphere moving at a velocity of 40 mm/yr toward the right over Gaussian heat sources with half widths of (*a*), 2000 km, (*b*) 200 km, and (*c*) 60 km. From top to bottom the boxes contain contours of temperature perturbation, surface heat flow, seafloor topography, free-air gravity anomaly and geoid height. The peak in each of the observable fields lies on the downstream side of the source.

6. Conclusions

1. A stationary, time-independent heat source, within a moving lithosphere, has been used to represent the upper

mantle heat transfer processes associated with material upwelling at a spreading center and lithospheric thinning over a hot spot. Using this heat source representation along with a linear thermomechanical model for the oceanic lithosphere, we have derived analytic expressions, in the Fourier transform domain, relating the three-dimensional heat source to fields that can be observed on the earth's surface (i.e., surface heat flow, seafloor topography, and geopotential). The linearity and computational simplicity of the model lends itself to transfer function modeling, forward modeling, and inverse modeling.

2. The results from gravity/topography transfer function modeling demonstrate that the thermal compensation model transfer function peaks at a wavelength greater than the flexural wavelength; the transfer function peak for the regional compensation model occurs at a wavelength less than λ_f. This indicates that off-ridge thermotectonic features can be distinguished from off-ridge, regionally compensated topography on the basis of the gravity/topography transfer function. However, if a region of seafloor topography has a mixed compensation mechanism such as the Hawaiian swell and the Hawaiian-Emperor seamount chain, then near the flexural wavelength, the observed transfer function is difficult to interpret.

3. The utility of the heat source formulation was demonstrated by reproducing the thermal structure and observables for a plate cooling model. The heat flow–age and depth-age relations are in agreement with previous studies. Furthermore, we have shown that for typical spreading velocities, geoid height is almost entirely dependent upon age and agrees with geoid height relations derived using the Ockendon-Turcotte approximation.

4. The amplitudes of the surface observables for a mature lithosphere moving through a Gaussian heat source are dependent upon the width of the source. A very narrow source (half width of 60 km) does not appear strongly in the observable fields because the flexural rigidity of the lithosphere suppresses the signal. The geoid height is greatest over a broad source (half width of 2000 km), while the free-air gravity anomaly is most sensitive to an intermediate width source (half width of 200 km).

5. The relationship between the heat source and the observables is linear. Therefore, it is possible to invert directly for the class of sources that are consistent with the data by using linear inverse theory. The class can be narrowed by applying physically reasonable constraints. The three data types are each sensitive to different aspects of the heat source and should be used simultaneously in the inversion to enhance the source resolution. The inverse problem will divide the observed fields into a part that is associated with the lithosphere and a part that comes from deeper within the earth and hopefully will provide a characteristic wavelength for the off-ridge thermal perturbations.

Appendix A: Thermomechanical Response of a Moving Plate to a Distributed Heat Source

In this section we derive analytic expressions relating quantities that can be observed on the surface of the earth (i.e., surface heat flow, topography, geoid height, and free-air gravity anomaly) to a thermal perturbation within the lithosphere. The geometry of the problem is shown in Figure 1. The observable fields are perturbed as a plate of constant thickness l passes through a heat source $q(x, y, z)$ at a velocity $\mathbf{v}$. The temperature at the plate's surface is constant $T(x, y, 0) = T_0$ and at its base is $T(x, y, l) = T_m$. The assumed rheology and mechanical boundary conditions are described in section 2. The solution is obtained through a number of separate steps.

1. Solve the inhomogeneous time-independent heat conduction equation.
2. Differentiate the temperature with respect to z to determine the surface heat flow.
3. Integrate the thermally induced density perturbations to find the vertical stress on the elastic layer.
4. Solve the inhomogeneous biharmonic equation for the surface deflection.
5. Calculate the disturbing potential for the thermally compensated topography.

Each of these problems has been solved separately (for 1 and 2, see *Carslaw and Jaeger* [1959, p. 266] and *Birch* [1975]; for 3 and 4, see *Banks et al.* [1977] and *Dorman and Lewis* [1974]; for 5, see *Parker* [1972]). Space domain convolutions could be used to link these separate problems, but many of the convolution integrals must be performed numerically and require large amounts of computer time for even the simplest heat source geometries. Fourier transformation of all of the equations in the $\hat{x}$ and $\hat{y}$ directions reduces the space domain convolutions to wave number domain multiplications. The convolutions in the $\hat{z}$ direction are simple enough to be evaluated analytically.

From the outset, the homogeneous solution to the heat conduction problem is subtracted from the thermal structure, since this solution corresponds to the infinite wavelength case. All length scales are nondimensionalized by the lithospheric thickness l. Throughout the derivation the following notation is used:

$$\mathbf{x} = (x, y)$$

$$\mathbf{k} = (k_x, k_y)$$

$$\nabla_h = \frac{\partial}{\partial x} + \frac{\partial}{\partial y}$$

The two-dimensional Fourier transform and inverse transform are defined as

$$T(\mathbf{k}\, z) = \int_{-\infty}^{\infty}\int_{-\infty}^{\infty} t(\mathbf{x}, z) e^{i\mathbf{k}\cdot\mathbf{x}}\, d^2\mathbf{x}$$

$$t(\mathbf{x}, z) = \frac{1}{(2\pi)^2}\int_{-\infty}^{\infty}\int_{-\infty}^{\infty} T(\mathbf{k}, z) e^{-i\mathbf{k}\cdot\mathbf{x}} d^2\mathbf{k}$$

or in shorthand notation,

$$T(\mathbf{k}, z) = \mathcal{F}_2\,[t(\mathbf{x}, z)]$$

$$t(\mathbf{x}, z) = \mathcal{F}_2^{-1}[T(\mathbf{k}, z)]$$

Temperature

The temperature perturbation $t(\mathbf{x}, z)$ is found by solving

$$l\,\mathbf{v}\cdot\nabla_h t(\mathbf{x}, z) - \kappa\,\nabla_h^2 t(\mathbf{x}, z) - \kappa\,\frac{\partial^2 t(\mathbf{x}, z)}{\partial z^2} = \frac{l^2 q(\mathbf{x}, z)}{\rho_m C_p} \qquad \text{(A1)}$$

subject to the boundary conditions

$$t(\mathbf{x}, 0) = 0 \tag{A2}$$

$$t(\mathbf{x}, 1) = 0 \tag{A3}$$

where κ is the thermal diffusivity, ρ_m is the density, and C_p is the heat capacity. The boundary conditions are maintained if an infinite number of heat sources and sinks are suitably placed above and below the plate. Consider a source $q(\mathbf{x}, z) = q(\mathbf{x})\ \delta(z - z_0)$. By adding positive images at $z_0 + 2m$ and negative images at $-z_0 + 2m$, where m is any integer, the new source becomes

$$q(\mathbf{x}, z) = q(\mathbf{x}) \sum_{m=-\infty}^{\infty} [\delta(z - z_0 - 2m) - \delta(z + z_0 - 2m)] \tag{A4}$$

and the boundary conditions are satisfied. With this source, (A1) becomes

$$\frac{l}{\kappa}\,\mathbf{v} \cdot \nabla_h t - \nabla_h{}^2 t - \frac{\partial^2 t}{\partial z^2} = \frac{l^2 q(\mathbf{x})}{\kappa \rho_m C_P} \cdot \sum_{m=-\infty}^{\infty} [\delta(z - z_0 - 2m) - \delta(z + z_0 - 2m)] \tag{A5}$$

Fourier transformation of (A5) in the $\hat{x}$, $\hat{y}$, and $\hat{z}$ directions yields

$$\left[\left(\frac{-il}{\kappa}\,\mathbf{v} \cdot \mathbf{k} + \mathbf{k} \cdot \mathbf{k}\right) + k_z{}^2\right] T(\mathbf{k}, k_z) = \frac{l^2 q(\mathbf{k})}{\kappa \rho_m C_p}\left[(e^{ik_z z_0} - e^{-ik_z z_0}) \sum_{m=-\infty}^{\infty} e^{ik_z 2m}\right] \tag{A6}$$

where $q(\mathbf{k})$ is the Fourier transform of $q(\mathbf{x})$. Let

$$p^2 = \mathbf{k} \cdot \mathbf{k} - \frac{il}{\kappa}\,\mathbf{v} \cdot \mathbf{k} \tag{A7}$$

Next we solve (A6) for $T(\mathbf{k}, k_z)$ and take its inverse Fourier transform in the k_z direction only:

$$T(\mathbf{k}, z) = \frac{l^2 q(\mathbf{k})}{2\pi \kappa \rho_m C_p} \sum_{m=-\infty}^{\infty} \int_{-\infty}^{\infty} \exp [ik_z(z_0 - z + 2m)] - \exp [-ik_z(z_0 + z - 2m)][(k_z + ip)(k_z - ip)]^{-1}\, dk_z \tag{A8}$$

This integral is performed by calculus of residues. The poles lie at $\pm ip$ and never intersect the real axis except when $|\mathbf{k}| = 0$, which corresponds to the homogeneous solution. The path of integration is chosen so that temperature is zero far from the heat source (i.e., Re $(p) > 0$). However, the $m = 0$ term must be treated separately, since the path of integration depends on sgn $(z - z_0)$. After this integration, (A8) becomes

$$T(\mathbf{k}, z) = \frac{l^2 q(\mathbf{k})}{2\kappa \rho_m C_p p}\left[e^{-p|z_0 - z|} - e^{-p(z_0 + z)} + (e^{-p(z - z_0)} + e^{p(z - z_0)} - e^{-p(z_0 + z)} - e^{p(z_0 + z)}) \sum_{m=1}^{\infty} e^{-2pm}\right] \tag{A9}$$

Since the root Re $(p) > 0$ was chosen for the contour integration, it is easily shown, from the binomial theorem, that

$$\sum_{m=1}^{\infty} e^{-2pm} = \frac{e^{-2p}}{(1 - e^{-2p})} \tag{A10}$$

A vertical superposition of heat sources leads to

$$T(\mathbf{k}, z) = \int_0^1 q(\mathbf{k}, z_0)\, K_0(\mathbf{k}, z, z_0)\, dz_0 \tag{A11}$$

where the temperature response function is

$$K_0(\mathbf{k}, z, z_0) = \frac{l^2}{2\kappa \rho_m C_p p}\left[e^{-p|z_0 - z|} - e^{-p(z_0 + z)} + (e^{-p(z - z_0)} + e^{p(z - z_0)} - e^{-p(z_0 + z)} - e^{p(z_0 + z)})\,\frac{e^{-2p}}{(1 - e^{-2p})}\right] \tag{A12}$$

The locations of the source and its images are clear from the structure of (A12). The first two exponentials correspond to the source at $z = z_0$ and a sink at $z = -z_0$. The following terms contain all of the other image sources.

Surface Heat Flow

The surface heat flow is the thermal conductivity $(\kappa \rho_m C_p)$ multiplied by the surface temperature gradient:

$$Q(\mathbf{k}) = \frac{\kappa \rho_m C_p}{l}\,\frac{\partial T(\mathbf{k}, z)}{\partial z}\bigg|_0 \tag{A13}$$

Inserting (A11) into (A13), we find that

$$Q(\mathbf{k}) = \int_0^1 q(\mathbf{k}, z_0)\, K_1(\mathbf{k}, z_0)\, dz_0 \tag{A14}$$

where the surface heatflow response function is

$$K_1(\mathbf{k}, z_0) = l\left[e^{-pz_0} + (e^{-pz_0} - e^{pz_0})\,\frac{e^{-2p}}{(1 - e^{-2p})}\right] \tag{A15}$$

Vertical Stress From the Thermal Anomaly

Let $\rho(\mathbf{k}, z) = -\alpha \rho_m T(\mathbf{k}, z)$ be the thermally induced density perturbation. The vertical pressure is

$$P(\mathbf{k}) = \alpha \rho_m l g \int_0^1 T(\mathbf{k}, z)\, dz \tag{A16}$$

where g is the gravitational acceleration and $T(\mathbf{k}, z)$ is given in (A11).

Flexural Response of the Elastic Layer

The equation for the static equilibrium of a thin elastic plate subject to a vertical load is

$$\frac{D}{l^4}\,\nabla_h{}^4 w(\mathbf{x}) + \Delta \rho g\, w(\mathbf{x}) = P(\mathbf{x}) \tag{A17}$$

where $w(\mathbf{x})$ is the deflection of the seafloor in the $-z$ direction, D is the flexural rigidity, $\Delta\rho$ is the density difference across the earth's surface (e.g., $\Delta\rho = \rho_m - \rho_w$ for seafloor deformation, ρ_w is the seawater density), and $\rho(\mathbf{x})$ is the pressure. By taking the two-dimensional Fourier transform of (A17), inserting (A16), and solving for $W(k)$, we find that

$$W(\mathbf{k}) = \left(1 + \frac{D|\mathbf{k}|^4}{l^4 g(\rho_m - \rho_w)}\right)^{-1} \frac{\alpha\rho_m l}{(\rho_m - \rho_w)} \cdot \int_0^1 \int_0^1 q(\mathbf{k}, z_0)\, K_0(\mathbf{k}, z, z_0)\, dz\, dz_0 \quad \text{(A18)}$$

After integrating K_0 over z, the surface deformation is

$$W(\mathbf{k}) = \int_0^1 q(\mathbf{k}, z_0)\, K_2(\mathbf{k}, z_0)\, dz_0 \quad \text{(A19)}$$

where the topography response function is

$$K_2(\mathbf{k}, z_0) = \left(1 + \frac{D|\mathbf{k}|^4}{l^4 g(\rho_m - \rho_w)}\right)^{-1} \frac{\alpha l^3}{2\kappa(\rho_m - \rho_w)C_p p^2} \cdot \left[2 - 2e^{-pz_0} + e^{-p(1+z_0)} - e^{-p(1-z_0)} + (2 - e^{-p} - e^{p})(e^{pz_0} - e^{-pz_0}) \frac{e^{-2p}}{(1 - e^{-2p})}\right] \quad \text{(A20)}$$

Disturbing Potential

The gravitational potential of a region of density $\rho(\mathbf{x}, z)$ that has been deflected vertically by an amount $w(\mathbf{x})$ is [*Parker*, 1972]

$$U(\mathbf{k}, -s) = 2\pi G l \sum_{m=0}^{\infty} \frac{1}{m!} \left(\frac{|\mathbf{k}|}{l}\right)^{m-1} \cdot \int_0^1 \mathcal{F}_2\,[w^m(\mathbf{x})\, \rho(\mathbf{x}, z)]\, e^{-|\mathbf{k}|(z+s)}\, dz \quad \text{(A21)}$$

where $-s$ is the location of the observation plane and G is the gravitational constant. For our model $\rho(\mathbf{x}, z)$ is the sum of the linear density gradient, which corresponds to the homogeneous temperatures gradient, and the density associated with the thermal perturbation

$$\rho(\mathbf{x}, z) = \rho_m - \rho_w + \alpha\rho_m T_m(1 - z) - \alpha\rho_m t(\mathbf{x}, z) \quad \text{(A22)}$$

By inserting (A11) into (A22) and (A22) into (A21), discarding the terms containing α^2, α^3, $\cdots$, and integrating over z we find that the potential is

$$U = U_w + U_\rho \quad \text{(A23)}$$

The first term on the right is the potential caused by the deformation of the homogeneous density structure. The second term is the potential for the thermally induced density anomaly. As discussed in section 2, the factor

$$\frac{2n}{2n + 1} = \frac{2a|\mathbf{k}|}{2a|\mathbf{k}| + l} \quad \text{(A24)}$$

is included to partially correct for the earth's sphericity. The first term in (A23) is

$$U_w(\mathbf{k}, -s) = \int_0^1 q(\mathbf{k}, z_0)\, K_w(\mathbf{k}, -s, z_0)\, dz_0 \quad \text{(A25)}$$

where

$$K_w(\mathbf{k}, -s, z_0) = \left(1 + \frac{D|\mathbf{k}|^4}{l^4 g(\rho_m - \rho_w)}\right)^{-1} \frac{2\pi G a l^4 \alpha e^{-|\mathbf{k}|s}}{\kappa C_p p^2 (2a|\mathbf{k}| + l)} \cdot \left\{1 + \frac{\alpha\rho_m T_m}{(\rho_m - \rho_w)}\left[1 + \frac{1}{|\mathbf{k}|}(e^{-|\mathbf{k}|} - 1)\right]\right\} \cdot \left[2 - 2e^{-pz_0} + e^{-p(1+z_0)} - e^{-p(1-z_0)} + (2 - e^{-p} - e^{p}) \cdot (e^{pz_0} - e^{-pz_0}) \frac{e^{-2p}}{(1 - e^{-2p})}\right] \quad \text{(A26)}$$

There are two cases to be considered when $U_\rho(\mathbf{k}, s)$ is calculated: the downstream case, where $p \neq |\mathbf{k}|$, and the cross-stream case, where $p = |\mathbf{k}|$. The thermally induced part of the potential is

$$U_\rho(\mathbf{k}, -s) = \int_0^1 q(\mathbf{k}, z_0)\, K_\rho(\mathbf{k}, -s, z_0)\, dz_0 \quad \text{(A27)}$$

where

$$K_\rho(\mathbf{k}, -s, z_0) = \frac{-2\pi G a l^4 \alpha e^{-|\mathbf{k}|s}}{\kappa C_p (2a|\mathbf{k}| + l)p} \left\{\frac{2p}{p^2 - |\mathbf{k}|^2}(e^{-|\mathbf{k}|z_0} - e^{-pz_0}) + (e^{pz_0} - e^{-pz_0})\left[\left(\frac{2p}{p^2 - |\mathbf{k}|^2} - \frac{e^{-(p+|\mathbf{k}|)}}{p + |\mathbf{k}|} - \frac{e^{(p-|\mathbf{k}|)}}{p - |\mathbf{k}|}\right) \cdot \left(\frac{e^{-2p}}{1 - e^{-2p}}\right) - \frac{e^{-(p+|\mathbf{k}|)}}{(p + |\mathbf{k}|)}\right]\right\} \quad p \neq |\mathbf{k}| \quad \text{(A28a)}$$

$$K_\rho(\mathbf{k}, -s, z_0) = \frac{-2\pi G a l^4 \alpha e^{-|\mathbf{k}|s}}{\kappa C_p (2a|\mathbf{k}| + l)\mathbf{k}} \left\{z_0 e^{-|\mathbf{k}|z_0} - (e^{|\mathbf{k}|z_0} - e^{-|\mathbf{k}|z_0}) \cdot \left[\frac{e^{-2|\mathbf{k}|}}{2|\mathbf{k}|} + \left(1 + \frac{1}{2|\mathbf{k}|}(e^{-2|\mathbf{k}|} - 1)\right) \cdot \frac{e^{-2|\mathbf{k}|}}{(1 - e^{-2|\mathbf{k}|})}\right]\right\} \quad p = |\mathbf{k}| \quad \text{(A28b)}$$

The total disturbing potential is a vertical convolution of the heat source with the potential response function:

$$U(\mathbf{k}, -s) = \int_0^1 q(\mathbf{k}, z_0)\, K_3(\mathbf{k}, -s, z_0)\, dz_0 \quad \text{(A29)}$$

where K_3 is

$$K_3 = K_w + K_\rho \quad \text{(A30)}$$

APPENDIX B: RESPONSE FUNCTIONS FOR LITHOSPHERIC THINNING

The computation time for a model is substantially reduced if the vertical variation in the heat source is decoupled from the horizontal variation as shown in equation (2). Perhaps the most useful vertical source variation decreases linearly with depth between z_1 and 1 (see section 2, equation (3)) since this source can be convolved with the four response functions. Furthermore, this source function can be used to construct a spreading ridge model or a lithospheric-thinning model. In this appendix the vertical convolution integrals (A11), (A14), (A25), and (A29) are carried out analytically using the vertical source function (3). This procedure is mathematically simple since the most difficult integrands are of the form z^2e^{-pz}; however, it involves a considerable amount of algebra. The results of these convolutions are given below. Temperature perturbation for the depth range $z_1 < z < 1$ is

$$T(\mathbf{k}, z) = q(\mathbf{k})\, K_0'(\mathbf{k}, z) \tag{B1}$$

where the temperature response function is

$$K_0'(\mathbf{k}, z) = \frac{l^2}{2\kappa\rho_m C_p p^2}\left\{2(1-z) - (1-z_1)\,e^{-pz}\,(e^{pz_1} + e^{-pz_1} + \frac{e^{-pz}}{p}(e^{-pz_1} - e^{pz_1} - e^{-p}) + \frac{e^{-p(1-z)}}{p} + \frac{e^{-2p}(e^{pz} - e^{-pz})}{(1-e^{-2p})}\left[(1-z_1)(e^{pz_1} + e^{-pz_1}) + \frac{1}{p}(e^{pz_1} - e^{-pz_1} - e^{p} + e^{-p})\right]\right\} \tag{B2}$$

Similarly, the surface heat flow is $q(\mathbf{k})$ multiplied by the response function

$$K_1'(\mathbf{k}) = \frac{l}{p}\left\{(1-z_1)\left[e^{-pz_1} + \frac{e^{-2p}(e^{pz_1} + e^{-pz_1})}{(1-e^{-2p})}\right] + \frac{1}{p}\left[(e^{-p} - e^{-pz_1}) + \frac{e^{-2p}}{(1-e^{-2p})}\cdot(e^{pz_1} - e^{-pz_1} - e^{p} + e^{-p})\right]\right\} \tag{B3}$$

The topography response function is

$$K_2'(\mathbf{k}) = \frac{\alpha l^3}{2\kappa\,(\rho_m - \rho_w)C_p p^3}\left(1 + \frac{D|\mathbf{k}|^4}{g(\rho_m - \rho_w)}\right)^{-1}\cdot\left\{(1-z_1)\left[p(1-z_1) - 2e^{-pz_1} + (e^{pz_1} + e^{-pz_1})\cdot\left(e^{-p} - \frac{e^{-2p}}{(1-e^{-2p})}(2 - e^{p} - e^{-p})\right)\right] + \frac{1}{p}\left[2(e^{-pz_1} - e^{-p}) + (e^{pz_1} - e^{-pz_1} - e^{p} + e^{-p})\cdot\left(e^{-p} - \frac{e^{-2p}}{(1-e^{-2p})}(2 - e^{p} - e^{-p})\right)\right]\right\} \tag{B4}$$

Again the potential response function is the sum of two terms:

$$K_3'(\mathbf{k}) = K_w'(\mathbf{k}) + K_\rho'(\mathbf{k}) \tag{B5}$$

where the contribution from the topography is

$$K_w'(\mathbf{k}) = \frac{4\pi G a(\rho_m - \rho_w) l e^{-|\mathbf{k}|s}}{2a|\mathbf{k}| + l}\left\{1 + \frac{\alpha\rho_m T_m}{(\rho_m - \rho_w)}\cdot\left[1 + \frac{1}{|\mathbf{k}|}(e^{-|\mathbf{k}|} - 1)\right]\right\} K_2'(\mathbf{k}) \tag{B6}$$

and the contribution from the thinned portion of the lithosphere is

$$K_\rho'(\mathbf{k}) = \frac{-2\pi G a\alpha l^4\, e^{-|\mathbf{k}|s}}{(2a|\mathbf{k}| + l)\,\kappa C_p p}\left\{\frac{2p}{p^2 - |\mathbf{k}|^2}\left[(1-z_1)\left(\frac{e^{-|\mathbf{k}|z_1}}{|\mathbf{k}|} - \frac{e^{-pz_1}}{p}\right) + \frac{1}{|\mathbf{k}|^2}(e^{-|\mathbf{k}|} - e^{-|\mathbf{k}|z_1}) - \frac{1}{p^2}(e^{-p} - e^{-pz_1})\right] + \frac{1}{p}\left[\left(\frac{e^{-(p+|\mathbf{k}|)}}{p + |\mathbf{k}|} - \left(\frac{2p}{p^2 - |\mathbf{k}|^2} - \frac{e^{-(p+|\mathbf{k}|)}}{p + |\mathbf{k}|} - \frac{e^{(p-|\mathbf{k}|)}}{p - |\mathbf{k}|}\right)\cdot\frac{e^{-2p}}{(1-e^{-2p})}\right)\left((1-z_1)(e^{pz_1} + e^{-pz_1}) + \frac{1}{p}(e^{pz_1} - e^{-pz_1} - e^{p} + e^{-p})\right)\right]\right\} \tag{B7}$$

when $p \neq |\mathbf{k}|$, and is

$$K_\rho'(\mathbf{k}) = \frac{-2\pi G a\alpha l^4\, e^{-|\mathbf{k}|s}}{(2a|\mathbf{k}| + l)\,\kappa C_p|\mathbf{k}|^2}\left\{z_1(1-z_1)\,e^{-|\mathbf{k}|z_1} + \frac{1}{|\mathbf{k}|}(e^{-|\mathbf{k}|} + (1-2z_1)\,e^{-|\mathbf{k}|z_1}) + \frac{2}{|\mathbf{k}|^2}(e^{-|\mathbf{k}|} - e^{-|\mathbf{k}|z_1}) + \left[\frac{e^{-2|\mathbf{k}|}}{2|\mathbf{k}|} + \left(1 + \frac{1}{2|\mathbf{k}|}(e^{-2|\mathbf{k}|} - 1)\right)\frac{e^{-2|\mathbf{k}|}}{(1-e^{-2|\mathbf{k}|})}\right]\cdot\left[(1-z_1)(e^{|\mathbf{k}|z_1} + e^{-|\mathbf{k}|z_1}) + \frac{1}{|\mathbf{k}|}(e^{|\mathbf{k}|z_1} - e^{-|\mathbf{k}|z_1} - e^{|\mathbf{k}|} + e^{-|\mathbf{k}|})\right]\right\} \tag{B8}$$

when $p = |\mathbf{k}|$. The complex wave number p is

$$p = \mathbf{k}\cdot\mathbf{k} - \frac{il}{\kappa}(\mathbf{v}\cdot\mathbf{k}) \tag{B9}$$

FORTRAN code to generate models from these response functions can be obtained from the author.

Acknowledgments. I thank LeRoy Dorman for his many helpful suggestions and the reviewers for pointing out the weak points in the original manuscript. This work was supported by the NASA Geodynamics Program under grant NAG5152.

REFERENCES

Backus, G. E., and F. Gilbert, The resolving power of gross earth data, *Geophys. J. R. Astron. Soc., 16,* 169–205, 1968.

Banks, R. J., R. L. Parker, and S. P. Huestis, Isostatic compensation on a continental scale: Local versus regional mechanisms, *Geophys. J. R. Astron. Soc., 51,* 431–452, 1977.

Birch, F. S., Conductive heat flow anomalies over a hot spot in a moving medium, *J. Geophys. Res., 80,* 4825–4827, 1975.

Caldwell, J. G., and D. L. Turcotte, Dependence of the thickness of the elastic oceanic lithosphere on age, *J. Geophys. Res., 84,* 7572–7576, 1979.

Carslaw, H. S., and J. C. Jaeger, *Conduction of Heat in Solids,* 2nd ed., Oxford University Press, New York, 1959.

Chapman, M. E., and M. Talwani, Comparison of gravimetric geoids with Geos 3 altimetric geoid, *J. Geophys. Res., 84,* 3803–3816, 1979.

Chapple, W. M., and D. W. Forsyth, Earthquakes and bending of plates at trenches, *J. Geophys. Res., 84,* 6729–6749, 1979.

Cochran, J. R., and M. Talwani, Free-air gravity anomalies in the world's oceans and their relationship to residual elevation, *Geophys. J. R. Astron. Soc., 50,* 495–552, 1977.

Crough, S. T., Thermal origin of mid-plate hot-spot swells, *Geophys. J. R. Astron. Soc., 55,* 451–469, 1978.

Detrick, R. S., and S. T. Crough, Island subsidence, hot spots and lithospheric thinning, *J. Geophys. Res., 83,* 1236–1244, 1978.

Detrick, R. S., R. P. Von Herzen, S. T. Crough, D. Epp, and U. Fehn, Evidence for lithospheric reheating from heat flow measurements on the Hawaiian swell, *Nature, 292,* 142–143, 1981.

Dorman, L. M., and B. T. R. Lewis, Experimental isostasy, 1, Theory of the determination of the earth's isostatic response to a concentrated load, *J. Geophys. Res., 75,* 3357–3365, 1970.

Dorman, L. M., and B. T. R. Lewis, The use of nonlinear functional expansions in calculations of the terrain effect in airborne and marine gravimetry and gradiometry, *Geophysics, 39,* 33–38, 1974.

Gass, I. G., D. S. Chapman, H. N. Pollack, and R. S. Thorpe, Geological and geophysical parameters of mid-plate volcanism, *Philos. Trans. R. Soc. London, Ser. A., 288,* 581–597, 1978.

Hager, B. H., and R. J. O'Connell, A simple global model of plate dynamics and mantle convection, *J. Geophys. Res., 86,* 4843–4867, 1981.

Haxby, W. F., and D. L. Turcotte, On isostatic geoid anomalies, *J. Geophys. Res., 83,* 5473–5478, 1978.

Heestand, R. L., and S. T. Crough, The effect of hot spots on the oceanic depth-age relation, *J. Geophys. Res., 86,* 6107–6114, 1981.

Jeffreys, H., *The Earth,* 6th ed., Cambridge University Press, New York, 1976.

Kaula, W. M., Material properties for mantle convection consistent with observed surface fields, *J. Geophys. Res., 85,* 7031–7044, 1980.

Kirby, S. H., Tectonic stresses in the lithosphere: Constraints provided by the experimental deformation of rocks, *J. Geophys. Res., 85,* 6353–6363, 1980.

Lambeck, K., Gravity anomalies over ocean ridges, *Geophys. J. R. Astron. Soc., 30,* 37–53, 1972.

Lambeck, K., and S. M. Nakiboglu, Seamount loading and stress in the lithosphere, *J. Geophys. Res., 85,* 6403–6418, 1980.

Lewis, B. T. R., and L. M. Dorman, Experimental isostasy. 2, An isostatic model for the United States derived from gravity and topographic data, *J. Geophys. Res., 75,* 3367–3386, 1970.

Mammerickx, J., Depth anomalies in the Pacific: Active, fossil and precursor, *Earth Planet. Sci. Lett., 53,* 147–157, 1981.

McKenzie, D. P., Some remarks on heat flow and gravity anomalies, *J. Geophys. Res., 72,* 6261–6273, 1967.

McKenzie, D. P., Surface deformation, gravity anomalies and convection, *Geophys. J. Roy. Astron. Soc., 48,* 211–238, 1977.

McKenzie, D. P., and C. Bowin, The relationship between bathymetry and gravity in the Atlantic ocean, *J. Geophys. Res., 81,* 1903–1915, 1976.

McNutt, M., Compensation of oceanic topography: An application of the response function technique to the Surveyor area, *J. Geophys. Res., 84,* 7589–7598, 1979.

Menard, H. W., Depth anomalies and the bobbing motion of drifting islands, *J. Geophys. Res., 78,* 5128–5137, 1973.

Menard, H. W., and T. M. Atwater, Changes in direction of seafloor spreading, *Nature, 219,* 463–467, 1968.

Menard, H. W., and L. M. Dorman, Dependence of depth anomalies upon latitude and plate motion, *J. Geophys. Res., 82,* 5329–5335, 1977.

Ockendon, J. R., and D. L. Turcotte, On the gravitational potential and field anomalies due to thin mass layers, *Geophys. J. R. Astron. Soc., 48,* 479–492, 1977.

Oldenburg, D. W., A physical model for the creation of the lithosphere, *Geophys. J. R. Astron. Soc., 43,* 425–451, 1975.

Oldenburg, D. W., A comprehensive solution to the linear deconvolution problem, *Geophys. J. R. Astron. Soc., 65,* 331–357, 1981.

Parker, R. L., The rapid calculation of potential anomalies, *Geophys. J. R. Astron. Soc., 31,* 447–455, 1972.

Parker, R. L., Understanding inverse theory, *Annu. Rev. Earth Planet. Sci., 5,* 35–64, 1977.

Parker, R. L., and D. W. Oldenburg, Thermal model of ocean ridges, *Nature Phys. Sci., 242,* 137–139, 1973.

Parsons, B., and D. P. McKenzie, Mantle convection and the thermal structure of the plates, *J. Geophys. Res., 83,* 4485–4496, 1978.

Parsons, B., and F. M. Richter, A relation between driving forces and geoid anomaly associated with mid-ocean ridges, *Earth Planet. Sci. Lett., 51,* 445–450, 1980.

Parsons, B., and J. G. Sclater, An analysis of the variation of the ocean floor bathymetry and heat flow with age, *J. Geophys. Res., 82,* 803–827, 1977.

Pollack, H. N., I. G. Gass, R. S. Thorpe, and D. S. Chapman, On the vulnerability of the lithospheric plates to mid-plate volcanism: Reply to comments by P. R. Vogt, *J. Geophys. Res., 86,* 961–966, 1981.

Sandwell, D. T., and K. A. Poehls, A compensation mechanism for the Central Pacific, *J. Geophys. Res., 85,* 3751–3758, 1980.

Sandwell, D. T., and G. Schubert, Geoid height versus age for symmetric spreading ridges, *J. Geophys, Res., 85,* 7235–7241, 1980.

Schubert, G., C. Froidevaux, and D. A. Yuen, Oceanic lithosphere and asthenosphere: Thermal and mechanical structure, *J. Geophys. Res., 81,* 3525–3540, 1976.

Sclater, J. G., and J. Francheteau, The implications of terrestrial heat flow observations on current tectonic and geochemical models of the crust and upper mantle of the earth, *Geophys. J. R. Astr. Soc., 20,* 509–542, 1970.

Sclater, J. G., R. N. Anderson, and M. L. Bell, Elevation of ridges and evolution of the central eastern Pacific, *J. Geophys. Res., 76,* 7888–7915, 1971.

Sclater, J. G., L. A. Lawver, and B. Parsons, Comparison of long-wavelength residual elevation and free-air gravity anomalies in the North Atlantic and possible implications for the thickness of the lithospheric plate, *J. Geophys. Res., 80,* 1031–1052, 1975.

Sleep, N. H., and B. Rosendahl, Topography and tectonics of ridge axes, *J. Geophys. Res., 84,* 6831–6839, 1979.

Turcotte, D. L., and E. R. Oxburgh, Finite amplitude convection cells and continental drift, *J. Fluid Mech., 28,* 29–42, 1967.

Turcotte, D. L., and E. R. Oxburgh, Stress accumulation in the lithosphere, *Tectonophysics, 35,* 183–199, 1976.

Walcott, R. I., Flexure of the lithosphere at Hawaii, *Tectonophysics, 9,* 435–446, 1970.

Watts, A. B., An analysis of isostasy in the world's oceans, 1, Hawaiian-Emperor seamount chain, *J. Geophys. Res., 83,* 5989–6004, 1978.

(Received February 27, 1981;
revised October 2, 1981;
accepted October 16, 1981.)